LASER & PHOTONICS REVIEWS
www.lpr-journal.org

Single-Mode Electrically Pumped Terahertz Laser in an Ultracompact Cavity via Merging Bound States in the Continuum

Jieyuan Cui, Yunda Chua, Song Han, Chongwu Wang, Yuhao Jin, Jinghao Li, Yongquan Zeng, Qian Wang, Ming Ye, Wenduo Chen, Song Zhu, Fangyuan Sun, Lianhe Li, Alexander Giles Davies, Edmund Harold Linfield, Chuan Seng Tan, and Qi Jie Wang**

Photonic bound states in the continuum (BICs) are highly localized optical modes that have found important applications in lasers, sensors, modulators, and harmonic signal generators. While possessing a higher quality factor (Q) as compared to leaky photonic modes, regular BICs (e.g., either symmetry-protected or accidental BICs) normally require large cavity sizes and are usually sensitive to the fabrication imperfections that introduce lattice disorders. Moreover, the previous demonstrations of BIC lasers are mostly based on optical pumping and operated in the visible and near-infrared regimes. Here, an electrically pumped BIC laser is demonstrated by merging two types of BIC modes based on a quantum cascade chip in the terahertz (THz) regime, which has an ultra-compact size (with a pump area around $4\lambda^2$). The measured side-mode suppression ratio (SMSR) can reach up to ≈20 dB, indicating a good single-mode performance over the entire dynamic range. In addition, the emitted beam shows a nontrivial cylindrical vector beam profile, a typical topological feature of BIC lasers. This work would pave the way for practical use of the emerging BIC concepts in pursuing ultra-compact and high-performance electrically driven laser sources, which are highly desired in advanced optoelectronics and integrated photonics.

1. Introduction

Bound state in the continuum (BIC), first proposed as a mathematical concept in 1929 by von Neumann and Wigner, describes the wavefunction localization of particles inside the continuum space via a quantum interference mechanism.[1] After decades of exploration, it has attracted widespread attention in the classical wave systems,[2] such as acoustics, water waves, and photonics.[3–14] Photonic crystals could not only provide a clean and versatile platform for implementing different types of BICs but also can find practical applications in lasers,[15–19] sensors,[20,21] harmonic signal generators,[22,23] and so on. Among these advanced applications, photonic BIC laser draws extensive attention as one of the most promising applications of the BIC concept. A BIC laser can provide theoretically perfect vertical confinement due to modes symmetry mismatch or destructive interference, as well as strong in-plane feedback caused by small group velocities (as demonstrated in conventional band-edge lasers[24]). Thus, the photonic modes in a finite-size BIC cavity are amplified by the gain medium, and coupled to the continuum of free space through surface emission channels as laser radiation. However, as an

J. Cui, Y. Chua, C. Wang, Y. Jin, J. Li, M. Ye, W. Chen, S. Zhu, F. Sun, C. S. Tan, Q. J. Wang
Centre for OptoElectronics and Biophotonics, School of Electrical and Electronic Engineering & The Photonics Institute
Nanyang Technological University
Singapore 639798, Singapore
E-mail: qjwang@ntu.edu.sg

S. Han
ZJU-Hangzhou Global Scientific and Technological Innovation Center
Zhejiang University
Hangzhou 311215, China
E-mail: song.han@zju.edu.cn

The ORCID identification number(s) for the author(s) of this article can be found under https://doi.org/10.1002/lpor.202300350

DOI: 10.1002/lpor.202300350

S. Han
Interdisciplinary Center for Quantum Information, State Key Lab. of Modern Optical Instrumentation, College of Information Science and Electronic Engineering
Zhejiang University
Hangzhou 310027, China

Y. Zeng
Electronic Information School
Wuhan University
Wuhan 430072, China

Q. Wang
Institute of Materials Research and Engineering, Agency for Science Technology, and Research (A*STAR)
2 Fusionopolis Way, #08-03, Innovis 138634, Singapore

L. Li, A. G. Davies, E. H. Linfield
School of Electronic and Electrical Engineering
University of Leeds
Leeds LS2 9JT, UK

isolated BIC, the symmetry-protected BIC[15] or the accidental BIC[8] often suffers considerable Q factor reduction caused by mode broadening (in k-space) and scattering in actual devices with finite cavity size and fabrication imperfections.[25] Thus, most of the currently reported BIC lasers were based on cavities with substantially large sizes[26] (Table S1, Supporting Information) as compared to the lasing wavelength and highly precise fabrication processes.[27]

Furthermore, it is noted that most of the BIC lasers to date have been optically pumped (Table S1, Supporting Information), which is difficult for on-chip integration with photonic circuits. The realization of electrical pumping with a compact device footprint is urgently needed and of great significance for more practical applications in advanced optoelectronics and integrated photonics. In addition, although being extensively investigated in the visible and near-infrared (IR) regimes, the photonic BIC lasers have been rarely reported in longer wavelengths, e.g., mid-IR or terahertz (THz) regimes, which have important applications in the fields like wireless communication,[28] processing,[29] non-invasive/night-vision imaging,[30] and spectroscopy. As an electrically pumped semiconductor-based laser, quantum cascade lasers (QCLs) are the most important source of mid-IR and THz owing to their compactness, electrical pumping, and high efficiency.[31–36] In the THz regime, the photonic band edge modes,[37] defect modes,[38] or the 1D distributed feedback grating (DFB) device configurations[39] have been applied for engineering the lasing emissions of QCLs. However, they are usually sensitive to the overall device size and the structural disturbances that eventually lead to multimode emission or suffer from large or irregular beam divergence.[39,40] Therefore, advanced design concepts are highly desired to address these challenges.

Here, we experimentally demonstrate electrically pumped BIC lasers with miniaturized cavity sizes (with a pump area around $4\lambda^2$) based on THz QCLs platform in a merging BIC design.[25,27,41–44] The lasers with parameters around the "merging point" show excellent single-mode performance, with a side-mode suppression ratio (SMSR) of ≈20 dB. The surface-emitting (enabled by the topological nature of the BICs) single-mode lasers also present nontrivial vector beam features with low divergence (≈6°) and polarization singularity. For comparison, we also show that the isolated BIC lasers, with the lattice parameters deviating from the "merging point", show typical multimode lasing operations with the usage of the same QCL wafer.

2. Results and Discussion

2.1. Coexistence of Symmetry-Protected and Accidental BICs

The merging BIC laser cavity was constructed by drilling air holes through a three-well resonant-phonon GaAs/$Al_{0.15}Ga_{0.85}$As designed THz QCL wafer and its top contact gold layer (**Figure 1**a). The wafer thickness was measured to be ≈13.3 μm, and the refractive index n is ≈4.3, respectively. Such laser device only excites the TM-polarized (E_z) photonic modes as the configuration of double-metal claddings. Figure 1b shows the photonic band structure under periodic boundary conditions in 3D finite-element simulations (see Experimental Section). The radius of the air hole is $r = 6.9$ μm and the lattice period is $a = 23.8$ μm. The cavity supports leaky modes with finite lifetimes whose dispersion curves lie above the light cone. Among these, some peculiar discrete modes can appear with theoretically infinite Q factor at discrete k points due to symmetry incompatibility and mode destructive interference (so as called BICs). As shown in Figure 1c, we focus on the second TM band (golden line; denoted as TM_2) above the light cone. By design, the band edge frequency (≈2.95 THz) of the TM_2 mode is within the QCL wafer's gain bandwidth (≈2.7–3.1 THz; see Experimental Section and Figure S1, Supporting Information). Apart from the symmetry-protected BIC mode at the center of the Brillouin zone, two unremarkable points with divergent Q factor (accidental BICs) also appear at $k = \pm 0.032$ (π/a) (Figure 1d).

2.2. Evolution of BICs with the Variation of Structural Parameters

The distance between the accidental BICs and the symmetry-protected BIC in momentum space can be modulated by varying the system parameters.[27,41] **Figure 2**a shows the trajectories of BICs evolution in k-space with the variation of period a. As illustrated, the symmetry-protected BIC always exists at the Γ point, and the accidental BICs gradually approach the Γ point with the increase of periodicity from $a = 23.0$ μm. At $a = 24.0$ μm, these two types of BIC overlap with each other (denoted as "merging BIC"), and an isolated BIC reappears when we further increase a to 24.5 μm. Due to the mode broadening caused by structural imperfections or the finite-size effect, the BIC modes would mix with the surrounding low-Q modes, thus exhibiting a finite Q factor.[25] The accidental BICs which share similar electric field distributions on the same band (Figure S2, Supporting Information) located near the symmetry-protected BIC can effectively suppress their radiation losses from the leakage channels at off-Γ points, and the suppression effect would be strongly affected by the distance between them.[10,25,27] We extracted the Q factors of the symmetry-protected BIC modes at different periodicities (black dashed line in Figure 2a). As shown in Figure 2b, the Q factors gradually increase as the two types of BICs get closer and maximize (exceeds 1×10^{10}) around a pre-merging point[25] of $a = 23.8$ μm. Thereafter, the Q factor dropped rapidly when the BICs completely merged to be a regular isolated BIC (below 1×10^6). To explore the topological nature of this evolution, we picked four representative periodicities of $a = 23.6$ μm, 23.8 μm, 24.0 μm, and 24.5 μm (white dash line in Figure 2a). The zoomed-in band structure can be seen in Figure S3, Supporting Information. We then plot the polarization distributions of the far-field radiation together with the brightness map of the Q factors in momentum space in Figure 2c–f, respectively. The length and direction of the white short lines represent the intensity and polarization angle of the electric field. The polarization field forms a singularity at the center, which corresponds to the symmetry-protected BIC. The topological charge was calculated to be $q = +1$ by choosing a circle around the Γ point with $|k| = 0.01\pi$/a (see details in

Q. J. Wang
School of Physical and Mathematical Sciences
Nanyang Technological University
Singapore 637371, Singapore

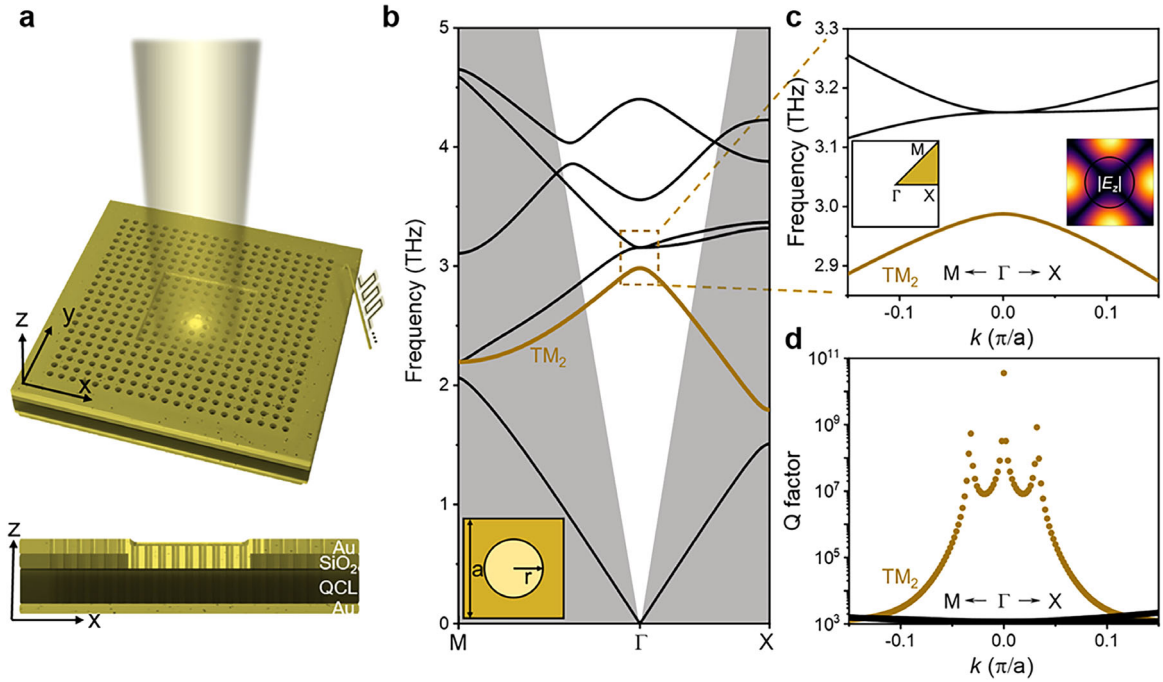

Figure 1. Coexistence of symmetry-protected and accidental BICs in a quantum cascade laser (QCL) platform. a) Schematic of the electrically pumped BIC lasers (top). The device cross-section configuration is Au/SiO_2/QCL/Au (bottom), where the two Au layers work as electrodes and modal confinement in the vertical direction with small Ohmic losses at terahertz frequencies, and only the central 9 by 9 periods without SiO_2 insulating layer were pumped. b,c) Band structure of the TM-polarized photonic modes calculated by 3D finite-element simulation. It is noted that QCLs intrinsically have TM-polarized light due to the intersubband transition nature. Here, we focus on the TM_2 band (golden line) which carries the quadrupole mode. The lattice constant of the unit cell used here is $a = 23.8$ μm with an air hole ($r = 6.9$ μm) in the center. d) Calculated Q factors of the three resonances shown in c, three high-Q modes coexist on the TM_2 band, where the middle one is symmetry-protected BIC at the Γ point and the other two are accidental BICs at $k = \pm 0.032$ (π/a).

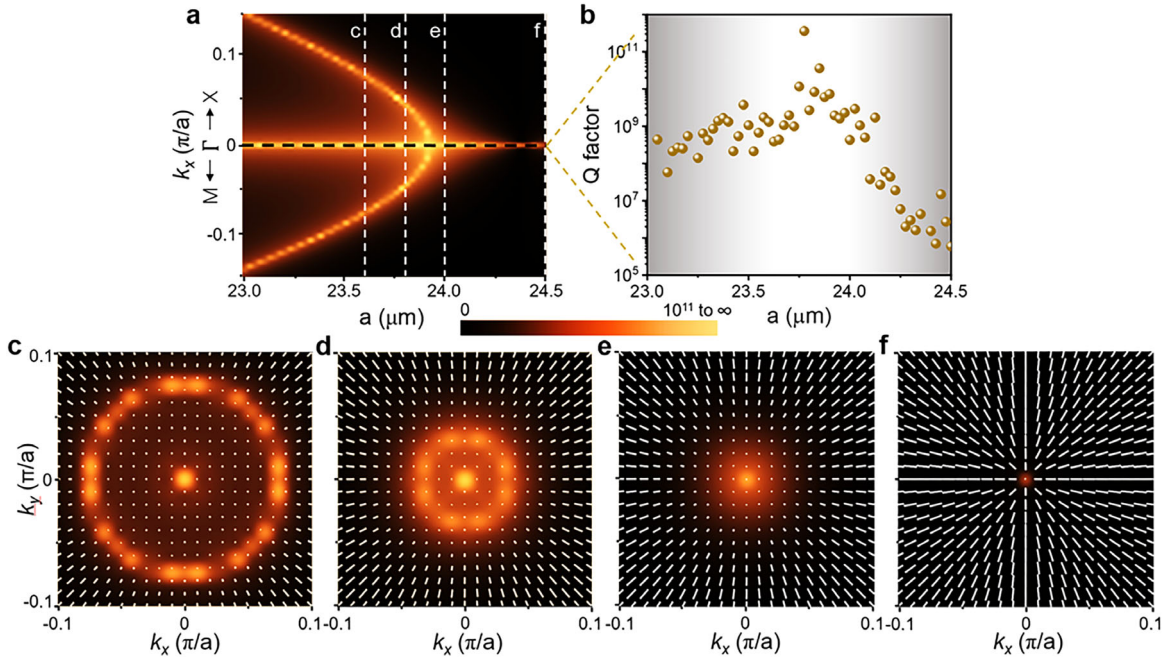

Figure 2. Simulated evolution of BICs in the momentum space. a) The evolution of Q factors for TM_2 band versus the lattice period a. The thickness of the active layer is 13.3 μm and the radius of the air hole is 6.9 μm. The color bar represents the Q factor. b) The calculated Q factor of the symmetry-protected BIC at the Γ point, corresponding to the black dash line in a. c–f), 2D Q factor and polarization map in momentum space around Γ point, for $a = 23.6$ μm, 23.8 μm, 24.0 μm, and 24.5 μm, respectively, with structural parameter corresponding to the white dash line in a. Multiple BICs (also polarization singularity) appear on the TM_2 band, and these BICs experience the evolution processes from shrinking to merging (denoted as "merging BIC"), and then annihilation.

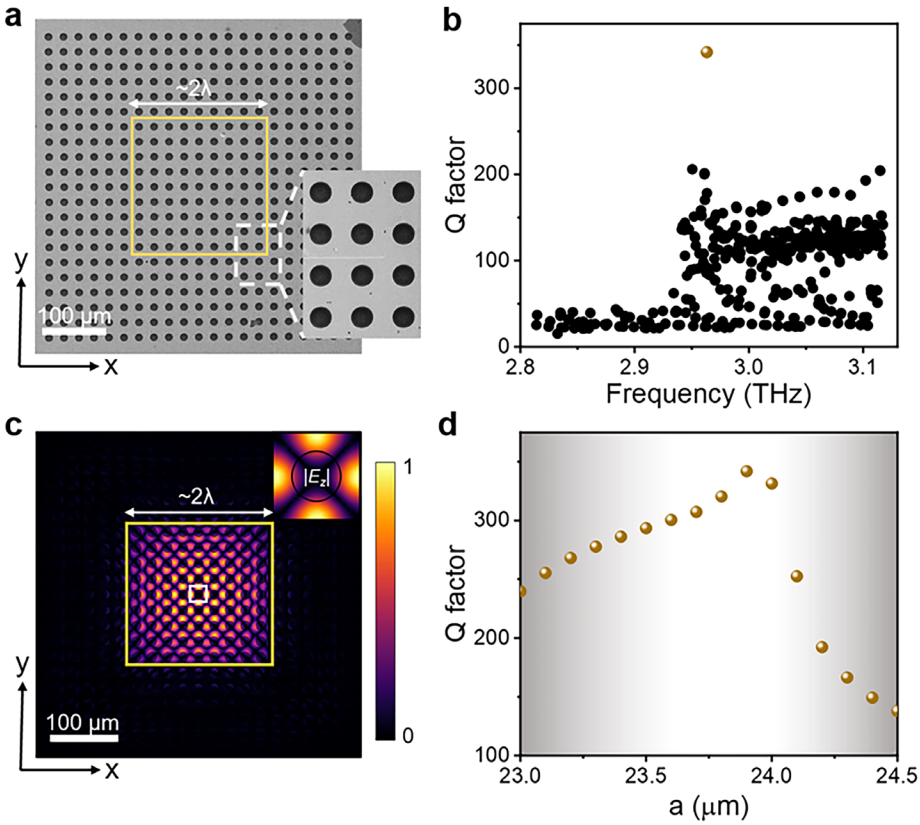

Figure 3. Fabricated mering QCL device structure and its simulations. a) Top view of the scanning electron microscope (SEM) image for the designed merging-BIC QCL. The central 9 by 9 periods inside the golden box are electrically pumped. Inset, magnified view of the edge of the pump region. b) Calculated Q factors of the eigenmodes corresponding to the structure as shown in (a). Here, the structural parameter is a = 23.9 μm, r = 6.9 μm, and the thickness is 13.3 μm. The unpumped region was set as a lossy dielectric with an imaginary part of 0.0159, obtained by the realistic material absorption losses of ≈20 cm^{-1}. c) The electric field of the high Q mode in (b). Inset, enlarged out-plane electric field distribution inside the white box. d) The Q factor of the BIC mode as a function of the lattice constant a, while the other structural parameters are the same as those used in (b).

Experimental Section). Besides, eight polarization singularities with opposite topological charges (consistent with charge conservation and C_{4v} symmetry) in Γ-X and Γ-M directions, corresponding to the accidental BICs,[25,27] exist and then disappear with the increase of a from 23.6 μm (Figure 2c) to 24.5 μm (Figure 2f) as a result of the topological charges annihilation. During this process, the overall winding number within $|k| = 0.01\pi/a$ as well as the far-field pattern is a conserved quality that is robust to the continuous parameter variation without changing the symmetry properties. As a consequence, this approach of BIC topological charges gives rise to a collective response (a larger core of polarization singularity) that can stand robustly against systematic disorders, structural imperfections, and photonic finite-size layouts, which is highly desired for laser applications. After merging, the core of polarization singularity becomes smaller, which returns to a regular isolated BIC, as shown in Figure 2f.

2.3. Laser Cavity Miniaturization

The numerical results above are all based on a unit cell with periodic boundary conditions (i.e., infinite size) along the x- and y-directions. For a real laser cavity, the device is always of finite size. **Figure 3**a shows the top view of a fabricated electrically pumped THz QCL, analyzed by scanning electron microscopy (SEM). The lattice constant is 23.9 μm and the radius of the air hole is 6.9 μm. The full laser cavity consists of 21 by 21 unit cells, while only the central 9 by 9 periods (within the golden square box) were electrically pumped (See details in Experimental Section). We then performed a 3D full-wave simulation to collect the Q factors based on this finite-size device (see Experimental Section). Two main reasons are considered for arranging such device configuration: first, the unpumped region is a lossy barrier that acts as a potential well[45] to effectively confine the BIC mode in the pump region (Figure 3c), and also obviously makes the laser device more energy efficient (i.e., less current injections); second, the pump region is much smaller than the overall photonic crystal size, avoiding the whisper-gallery-modes caused by gain spreading at the interface of the photonic cavity (unpatterned region).[46] As depicted in Figure 3b, only one mode with a relatively high Q factor was achieved over the mostly entire gain range of the QCL. The electric field profile of this high-Q mode (Figure 3c) is tightly confined in the pump region. Even at the finite-size layout, the photonic translation symmetry guarantees a quadrupole mode distribution, as shown in the inset of Figure 3c, which is consistent with the result in Figure 1c. To demonstrate the role of BICs manipulation in obtaining such a high-Q mode, we plot the Q factor as a function of lattice periodicity (Figure 3d). The Q

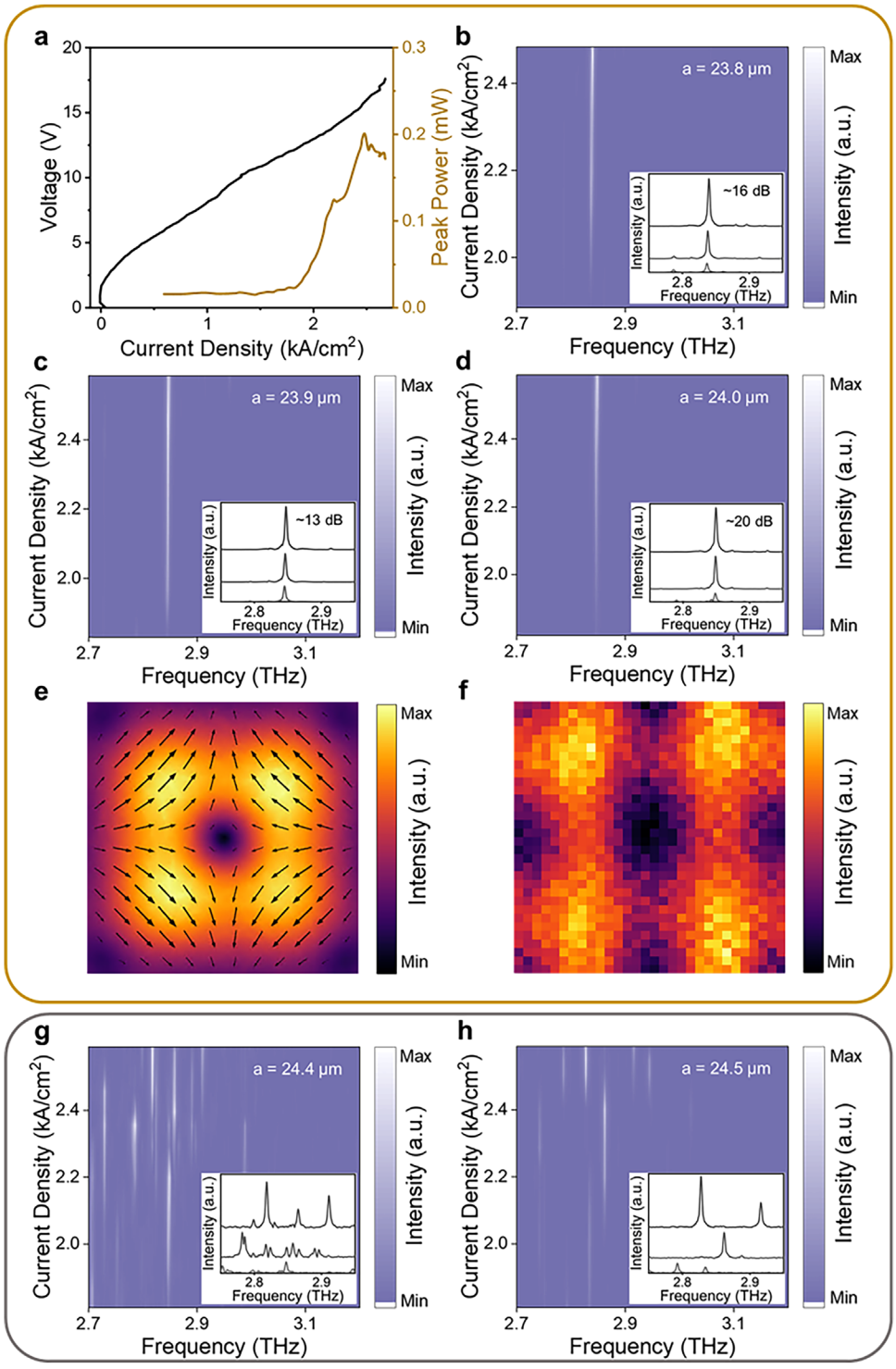

Figure 4. Lasing characteristics of the BIC lasers. a) Light-current-voltage curve of a BIC laser with lattice constant of $a = 23.8$ μm. The kinks in the graph are due to mode hopping in the device. The current difference between the discontinuity of the current-voltage curve (≈1.3 kA cm^{-2}) and the onset of the light (≈1.75 kA cm^{-2}) should come from the additional scattering and radiation losses induced by the residues on the side wall of photonic crystal air holes which were formed during the deep dry-etching fabrication process. b–d) 2D emission spectra mapping under different pump current densities of the BIC lasers with lattice constant close to or at the "merging BIC" point of b) $a = 23.8$ μm, c) $a = 23.9$ μm, and d) $a = 24.0$ μm, respectively. Inset, laser spectra measured under several typical pump current densities before the QCL rollover. The SMSR was calculated as seen in Figure S5, Supporting Information. e) Simulated far-field image and the polarization direction of the "merging BIC" mode with the lattice constant of $a = 24.0$ μm. f) Measured far-field image of the as-prepared BIC QCL with the lattice constant of $a = 24.0$ μm. The pump current density is 2.5 kA cm^{-2}. g,h) 2D mapping of the emission spectra under different pump current densities of the "isolated BIC" lasers with lattice constant of $a = 24.4$ μm and 24.5 μm.

factor first increases gradually (i.e., pre-merging state), reaches a maximum (≈342) at $a = 23.9$ μm (merging state), and then drops abruptly (after merging). The numerical results for both finite-size cavity and unit cell with periodic boundary conditions (Figure 2b) share the same trajectory, which directly implies that the merging BIC indeed gives rise to the highest cavity Q factor and tightest field localization. We note that the device parameters applied here are all carefully tuned based on a comprehensive consideration of cavity size and the imaginary free spectral range (Figure S6, Supporting Information).

2.4. Measurement of BIC Lasers

To experimentally demonstrate whether the near-merging BIC can ambiguously enhance the laser performances, we characterized a series of BIC lasers with different lattice parameters a. The devices were electrically pumped as depicted in Figure 1a (see details in Experimental Section). **Figure 4**a shows the experimental light-current-voltage curves at ≈8.6 K of a representative QCL device ($a = 23.8$ μm) with the highest Q factor of ≈320 as shown in Figure 3d. The lasing threshold is ≈1.8 kA cm^{-2}, and the rollover current density is ≈2.5 kA cm^{-2}. The emission spectra of this device at various pumping current densities were collected by using an FTIR with a DTGS THz detector (Figure 4b). The results show that the device exhibits good single-mode performance over a wide current density range (with an SMSR of ≈16 dB). The spectrum is gradually blue-shifted with increasing pumping, due to the Stark shift of the intersubband transition in the THz QCL medium.[47] Further characterization of the devices with lattice parameters around "merging BIC", such as $a = 23.9$ μm and $a = 24.0$ μm, are also presented in Figure 4c,d, respectively. The light-current-voltage curves of these two devices can be seen in Figure S4, Supporting Information. As expected, these lasers all exhibited single-mode lasing with the best SMSR performance of ≈20 dB (see details in Figure S5, Supporting Information). To confirm that the single-mode lasing originates from the theoretically predicted merging BIC mode, the far-field beam profile was measured for $a = 24.0$ μm (Figure 4f). A four-fold symmetric beam profile together with the intensity singularity at the center matches well with the simulated far-field pattern based on the actual device. The topological charge of the BIC mode calculated from the far field is $q = -1$ (Figure 4e). In comparison, the "isolated BIC" lasers with lattice periodicities that deviate from the "merging BIC", here select $a = 24.4$ μm and $a = 24.5$ μm as examples, which possess low-Q factors (Figure 3d and Figure S7, Supporting Information), exhibit multimode operation, as shown in Figure 4g,h, respectively. Indeed, it is easily observed that only the near-merging state can give rise to the best laser performance with largest SMSR and clearest far-field beam profile. All results indicate that the "merging BIC" mode is an ideal candidate for pursuing ultra-compact single-mode lasers.

3. Conclusion

In this work, we have demonstrated electrically pumped lasers working in the THz regime based on the merging BICs mechanism. The lasers can exhibit excellent single-mode operation even with a small cavity size (with a pump area around $4\lambda^2$), realized by merging the regular symmetry-protected BIC and the accidental BICs. The presence of off-Γ BICs close to the Γ-point (so as called "merging") can effectively enhance the Q factor by suppressing the radiation loss caused by the finite cavity size or fabrication imperfections in the lasers. Our electrically pumped merging BIC laser shed the light on promotion of practical applications of the BIC concepts in developing energy-efficient and monolithic ultra-compact light sources, together with the topological nature of the laser beam, making it a promising platform in wireless communication, non-invasive/night-vision imaging, molecular finger-print sensing, and many other advanced applications.

4. Experimental Section

Numerical Calculation: All the simulation results in this work were calculated based on a commercial finite element method software COMSOL Multiphysics. 3D simulations were calculated by using the eigenfrequency solver to get the band structures, eigenmodes, and Q factors at each k point of the BIC photonic crystals. The unit cell was cubic with a circular air hole drilled through the 13.3-μm-thick dielectric active layer. Periodic condition was imposed in the x–y plane. For the full structure simulation, the centered 9 by 9-unit cells which were pumped in real devices were treated as lossless, and the remaining unpumped region was set as a lossy dielectric with the imaginary part of 0.0159. The refractive index of the active layer was set as 4.29 with two perfect electric conductor layers at the top and bottom to extract the TM mode. Scattering boundary conditions were used to make a boundary transparent and avoid back reflection for the outgoing waves.

The topological charges (q) of the BICs were determined by the winding number of the polarization vectors shown in Figure 2c–f following the equation below,[7]

$$q = \frac{1}{2\pi} \oint_C dk \cdot \nabla_{\mathbf{k}} \phi(k) \tag{1}$$

Where C is the closed path with a counterclockwise direction surrounding a BIC. $\phi(k) = \arg[c_x(k) + ic_y(k)]$ was the polarization angle at each k, and c_x and c_y are the coefficients of far-field radiation with electric fields along the x and y directions, respectively.

Device Fabrication: The BIC laser cavities were designed on a three-well resonant-phonon GaAs/$Al_{0.15}Ga_{0.85}As$ THz QCL wafer. The gain bandwidth of the wafer was measured to be ≈2.7–3.1 THz (Figure S1, Supporting Information), with a ≈13.3 μm-thickness active region. The refractive index was calculated to be $n \approx 4.29$. The unpumped region was realized by inserting a SiO_2 insulating layer between the top contact Au and the THz emission layers.

Ti (15 nm)/Au (700 nm) metal layers were first deposited on the n^+ doped GaAs substrate and the THz QCL wafer by using an electron-beam evaporator, followed by the Au/Au thermo-compression wafer bonding to form the bottom contact Au layer. The QCL wafer substrate was thinned to below 80 μm by a polishing instrument. The residual GaAs substrate and $Al_{50}Ga_{50}As$ etch stop layers were then removed by a wet etching process with $NH_3 \cdot H_2O/H_2O_2/H_2O$ (3/55/32 mL) and hydrofluoric acid (49%) solution, respectively. Now the QCL active region was exposed. The processing of the BIC cavities was started with a SiO_2 (200 nm) insulating layer deposition. The pumping area was defined by optical lithography and reactive-ion etching (RIE) to remove the SiO_2 layer above the central 9 by 9 periods. The photonic crystal structure was then defined on the QCL wafer by optical lithography, followed by deposition and lift-off of contact layers (Ti/Au/Ti/SiO_2, 15/450/15/450 nm) on top of the air hole region. With the contact layers in the remaining area acting as a hard mask, The photonic structures were obtained by reactive-ion dry etching through the

active region with a gas mixture of $Cl_2/BCl_3/CH_4 = 5/100/20$ standard cubic centimeters per minute. SiO_2 was consumed during this process, and the remnant Ti/Au layer (≈200 nm) would be the top contact for current injection. The host substrate was thinned by a polisher to ≈200 μm and a Ti/Au layer (15/200 nm) was deposited as bottom electrode. Finally, the as-prepared sample was cleaved, indium-soldered onto a copper pedestal, wire-bonded, and attached to a cold finger in a cryostat for measurement.

Device Characterization: The fabricated BIC THz QCLs were fixed in a helium-gap-steam cryostat system with a temperature of ≈8.6 K. For the spectra measurement, the lasers were pumped by an electrical pulse generator (repetition rate of 10 kHz and pulse width of 500 ns). The laser spectra were collected by a Bruker Vertex 80 Fourier-transform infrared (FTIR) spectrometer with a room-temperature deuterated-triglycine sulfate (DTGS) detector. The spectra resolution was 0.08 cm^{-1}.

The far-field image of the "merging BIC" QCL was obtained by collecting the beam intensity with a THz Golay cell detector (TYDEX GC-1T). The detector with a collection aperture diameter of 11 mm was mounted on a mechanical arm with a scan step of 1 mm. A focal lens was used to collimate the laser beam. Here, the pulse width was increased to 800 ns and a 15 Hz electrical modulation was applied to lock in the amplified signal.

Supporting Information

Supporting Information is available from the Wiley Online Library or from the author.

Acknowledgements

This work was supported by funding from the Singapore Ministry of Education (MOE, grant no. MOE-T2EP50120-0009), A*STAR Programmatic Funds (A18A7b0058), and the National Research Foundation Competitive Research Program (NRF-CRP19-2017-01 and NRF-CRP23-2019-0007). L.L., A.G.D., and E.H.L. acknowledge the support of the EPSRC (UK) HyperTerahertz program (EP/P021859/1) and the Royal Society and the Wolfson Foundation.

Conflict of Interest

The authors declare no conflict of interest.

Author Contributions

J.C. and Y.C. contributed equally to this work. Q.W. supervised the work. J.C., S.H., and Q.W. conceived the idea of this work. J.C. did the numerical simulation with the help of S.H.; J.C. carried out the device fabrication with the help of Y.C.; and J.C. carried out the TEM characterizations. J.C. performed the QCL spectra and far-field measurement with the help of S.H. and Y.C.; L.L., A.G.D., and E.H.L. performed QCL wafer growth. Y.Z., Q.W., and C.T. helped with the wafer bonding. Q.W., J.C., and S.H. wrote the first draft of the manuscript. S.H. and Y.C. participated in data analysis. All authors discussed the results and commented on the manuscript.

Data Availability Statement

All simulation or experimental data in this paper are available from the corresponding authors under reasonable request.

Keywords

BIC lasers, electrical pumping, single-mode, ultra-compact sizes

Received: April 23, 2023
Revised: July 14, 2023
Published online:

[1] J. Von Neumann, E. Wigner, *Phys. Z* **1929**, *30*, 465.
[2] C. W. Hsu, B. Zhen, A. D. Stone, J. D. Joannopoulos, M. Soljačić, *Nat. Rev. Mater.* **2016**, *1*, 16048.
[3] R. Porter, D. Evans, *Wave Motion* **2005**, *43*, 29.
[4] C. Linton, P. McIver, *Wave Motion* **2007**, *45*, 16.
[5] X. Yin, J. Jin, M. Soljacic, C. Peng, B. Zhen, *Nature* **2020**, *580*, 467.
[6] B. Wang, W. Liu, M. Zhao, J. Wang, Y. Zhang, A. Chen, F. Guan, X. Liu, L. Shi, J. Zi, *Nat. Photonics* **2020**, *14*, 623.
[7] B. Zhen, C. W. Hsu, L. Lu, A. D. Stone, M. Soljacic, *Phys. Rev. Lett.* **2014**, *113*, 257401.
[8] C. W. Hsu, B. Zhen, J. Lee, S. L. Chua, S. G. Johnson, J. D. Joannopoulos, M. Soljacic, *Nature* **2013**, *499*, 188.
[9] S. Han, L. Cong, Y. K. Srivastava, B. Qiang, M. V. Rybin, A. Kumar, R. Jain, W. X. Lim, V. G. Achanta, S. S. Prabhu, Q. J. Wang, Y. S. Kivshar, R. Singh, *Adv. Mater.* **2019**, *31*, 1901921.
[10] Y. Ren, P. Li, Z. Liu, Z. Chen, Y.-L. Chen, C. Peng, J. Liu, *Sci. Adv.* **2022**, *8*, eade8817.
[11] M.-S. Hwang, K.-Y. Jeong, J.-P. So, K.-H. Kim, H.-G. Park, *Commun. Phys.* **2022**, *5*, 106.
[12] V. Ardizzone, F. Riminucci, S. Zanotti, A. Gianfrate, M. Efthymiou-Tsironi, D. G. Suàrez-Forero, F. Todisco, M. De Giorgi, D. Trypogeorgos, G. Gigli, K. Baldwin, L. Pfeiffer, D. Ballarini, H. S. Nguyen, D. Gerace, D. Sanvitto, *Nature* **2022**, *605*, 447.
[13] M. Minkov, I. A. D. Williamson, M. Xiao, S. Fan, *Phys. Rev. Lett.* **2018**, *121*, 263901.
[14] W. Ye, Y. Gao, J. Liu, *Phys. Rev. Lett.* **2020**, *124*, 153904.
[15] A. Kodigala, T. Lepetit, Q. Gu, B. Bahari, Y. Fainman, B. Kante, *Nature* **2017**, *541*, 196.
[16] Y. Wang, Y. Fan, X. Zhang, H. Tang, Q. Song, J. Han, S. Xiao, *ACS Nano* **2021**, *15*, 7386.
[17] J. H. Yang, Z. T. Huang, D. N. Maksimov, P. S. Pankin, I. V. Timofeev, K. B. Hong, H. Li, J. W. Chen, C. Y. Hsu, Y. Y. Liu, T. C. Lu, T. R. Lin, C. S. Yang, K. P. Chen, *Laser Photonics Rev.* **2021**, *15*, 2100118.
[18] C. Huang, C. Zhang, S. Xiao, Y. Wang, Y. Fan, Y. Liu, N. Zhang, G. Qu, H. Ji, J. Han, *Science* **2020**, *367*, 1018.
[19] X. Zhang, Y. Liu, J. Han, Y. Kivshar, Q. Song, *Science* **2022**, *377*, 1215.
[20] X. Chen, W. Fan, H. Yan, *Opt. Express* **2020**, *28*, 17102.
[21] L. Kuhner, L. Sortino, R. Berte, J. Wang, H. Ren, S. A. Maier, Y. Kivshar, A. Tittl, *Nat. Commun.* **2022**, *13*, 4992.
[22] N. Bernhardt, K. Koshelev, S. J. White, K. W. C. Meng, J. E. Froch, S. Kim, T. T. Tran, D.-Y. Choi, Y. Kivshar, A. S. Solntsev, *Nano Lett.* **2020**, *20*, 5309.
[23] Z. Liu, J. Wang, B. Chen, Y. Wei, W. Liu, J. Liu, *Nano Lett.* **2021**, *21*, 7405.
[24] H. Matsubara, S. Yoshimoto, H. Saito, Y. Jianglin, Y. Tanaka, S. Noda, *Science* **2008**, *319*, 445.
[25] M. S. Hwang, H. C. Lee, K. H. Kim, K. Y. Jeong, S. H. Kwon, K. Koshelev, Y. Kivshar, H. G. Park, *Nat. Commun.* **2021**, *12*, 4135.
[26] Z. Wang, Y. Liang, M. Beck, G. Scalari, J. Faist, *Phy. Rev. B* **2020**, *102*, 045122.
[27] J. Jin, X. Yin, L. Ni, M. Soljacic, B. Zhen, C. Peng, *Nature* **2019**, *574*, 501.
[28] S. S. Dhillon, C. Sirtori, J. Alton, S. Barbieri, A. De Rossi, H. E. Beere, D. A. Ritchie, *Nat. Photonics* **2007**, *1*, 411.
[29] J. Gao, J. Hovenier, Z. Yang, J. Baselmans, A. Baryshev, M. Hajenius, T. Klapwijk, A. Adam, T. Klaassen, B. Williams, *Appl. Phy. Lett.* **2005**, *86*, 244104.
[30] P. Dean, A. Valavanis, J. Keeley, K. Bertling, Y. Lim, R. Alhathlool, A. Burnett, L. Li, S. Khanna, D. Indjin, *J. Phys. D: Appl. Phys.* **2014**, *47*, 374008.
[31] A. Khalatpour, A. K. Paulsen, C. Deimert, Z. R. Wasilewski, Q. Hu, *Nat. Photonics* **2020**, *15*, 16.

[32] J. Faist, F. Capasso, D. L. Sivco, C. Sirtori, A. L. Hutchinson, A. Y. Cho, *Science* **1994**, *264*, 553.
[33] Y. Zeng, U. Chattopadhyay, B. Zhu, B. Qiang, J. Li, Y. Jin, L. Li, A. G. Davies, E. H. Linfield, B. Zhang, Y. Chong, Q. J. Wang, *Nature* **2020**, *578*, 246.
[34] G. Liang, X. Hu, X. Yu, Y. Shen, L. H. Li, A. G. Davies, E. H. Linfield, H. K. Liang, Y. Zhang, S. F. Yu, Q. J. Wang, *ACS Photonics* **2015**, *2*, 1559.
[35] G. Liang, Y. Zeng, X. Hu, H. Yu, H. Liang, Y. Zhang, L. Li, A. G. Davies, E. H. Linfield, Q. J. Wang, *ACS Photonics* **2017**, *4*, 517.
[36] Y. Zeng, B. Qiang, Q. J. Wang, *Adv. Opt. Mater.* **2019**, *8*, 1900573.
[37] Y. Chassagneux, R. Colombelli, W. Maineult, S. Barbieri, H. E. Beere, D. A. Ritchie, S. P. Khanna, E. H. Linfield, A. G. Davies, *Nature* **2009**, *457*, 174.
[38] A. Klimont, A. Ottomaniello, R. Degl'Innocenti, L. Masini, F. Bianco, Y. Wu, Y. D. Shah, Y. Ren, D. S. Jessop, A. Tredicucci, H. E. Beere, D. A. Ritchie, *J. Appl. Phys.* **2019**, *126*, 153104.
[39] Y. Jin, L. Gao, J. Chen, C. Wu, J. L. Reno, S. Kumar, *Nat. Commun.* **2018**, *9*, 1407.
[40] G. Liang, H. Liang, Y. Zhang, L. Li, A. G. Davies, E. Linfield, S. F. Yu, H. C. Liu, Q. J. Wang, *Opt. Express* **2013**, *21*, 31872.
[41] M. Kang, L. Mao, S. Zhang, M. Xiao, H. Xu, C. T. Chan, *Light: Sci. Appl.* **2022**, *11*, 228.
[42] M. Kang, S. Zhang, M. Xiao, H. Xu, *Phys. Rev. Lett.* **2021**, *126*, 117402.
[43] Z. Chen, X. Yin, J. Jin, Z. Zheng, Z. Zhang, F. Wang, L. He, B. Zhen, C. Peng, *Sci. Bull.* **2022**, *67*, 359.
[44] Z. Chen, X. Yin, P. Li, Z. Zheng, Z. Zhang, F. Wang, C. Peng, *Opt. Express* **2022**, *30*, 14033.
[45] X. Gao, L. Yang, H. Lin, L. Zhang, J. Li, F. Bo, Z. Wang, L. Lu, *Nat. Nanotechnol.* **2020**, *15*, 1012.
[46] Q. J. Wang, C. Yan, N. Yu, J. Unterhinninghofen, J. Wiersig, C. Pflugl, L. Diehl, T. Edamura, M. Yamanishi, H. Kan, F. Capasso, *Proc. Natl. Acad. Sci. USA* **2010**, *107*, 22407.
[47] S. Fathololoumi, E. Dupont, C. Chan, Z. Wasilewski, S. Laframboise, D. Ban, A. Mátyás, C. Jirauschek, Q. Hu, H. Liu, *Opt. Express* **2012**, *20*, 3866.